

Dual-Band Dual-Polarized Microstrip Antenna Array Using Double-Layer Gridded Patches for 5G Millimeter-Wave Applications

Wangyu Sun¹, Graduate Student Member, IEEE, Yue Li¹, Senior Member, IEEE, Le Chang¹, Member, IEEE, Hao Li¹, Xu Qin¹, and Hanyang Wang, Fellow, IEEE

Abstract—This article presents a dual-band and dual-polarized microstrip antenna array with broadside beam scanning ability for millimeter-wave applications. Within a compact multilayer structure, wide bandwidth and high port isolation are achieved by using double-layer gridded patches with three groups of metallic via-fences. For beam scanning purpose, a prototype of 2×2 array is designed, fabricated, and tested. The experimental results agree well with the simulations. For both orthogonal polarizations, the -10 dB bandwidth covers 23.3–31.7 and 42.5–46.5 GHz with average gains of 12 and 13.1 dBi, respectively. A 3 dB beam scanning angle from -51° to 43° at 27 GHz and -28° to 30° at 45 GHz is obtained. The proposed array provides dual-band and wideband properties for dual orthogonal polarizations with competitive beam steering range and compact dimensions, as a feasible solution for fifth-generation (5G) millimeter-wave mobile communications.

Index Terms—Antenna diversity, antenna radiation pattern, microstrip antennas, multiple frequency antennas.

I. INTRODUCTION

WITH the rapid development of the fifth-generation (5G) communication, stricter requirements on high data rate, large channel capacity, and low latency transmission attract researchers' attention to millimeter-wave (mmW) techniques [1]–[4]. Several mmW bands, for instance, spectra around 28, 38, 45, and 60 GHz, have been assigned for 5G development [5]–[9] and many works focused on these bands have been proposed for mobile handsets and

base stations [10]–[14]. Recently, according to different system requirements, mmW ultra-wideband antennas [15]–[18] or multiband antennas [19]–[32] are widely investigated to cover two or more frequency bands simultaneously for the expansion of available spectrums. They also save the occupied space and fabricated cost due to their high integration. This article mainly focuses on dual-band performances which avoid interferences with allocated or undesired bands [33]. One general way to achieve dual-band antennas is to combine two independent elements operating at different bands together [20]–[24]. Another method for dual-band antenna is to achieve dual modes operating at different frequencies [25]–[32]. The dual-polarized antenna is also widely investigated and applied for addressing the problems of heavily increased path loss and multipath fading in mmW frequency bands. Microstrip antennas and crossed-dipole antennas are two typical ways for dual polarizations [34]–[38]. However, quite a few researches on dual-band dual-polarized (DBDP) antennas, especially for mmW frequency, are reported in the state-of-the-art literature [39]–[45]. The stacked printed dipoles driven by a pair of differential ports are fabricated with a bandwidth of 11.4% and 5.1% [41]. In [42], by utilizing a square ring and a square patch fed by microstrip feeding lines, a DBDP antenna element is realized with a bandwidth of 1.4% (27.88–28.28 GHz) and 1.8% (38.56–39.28 GHz). For obtaining the scalability of a DBDP antenna array, dual off-center-fed dipoles are adopted in [45]. Finally, a 2×2 array is tested, covering bandwidths of 27.2–30.2 and 35.7–40.3 GHz with the peak gains of 13.1 and 13.2 dBi. To achieve wider bandwidths, metasurface-based broadband microstrip antennas have become a research hotspot recently [46]–[48]. On this basis, dual-band single-polarized antenna element [30] and DBDP antenna array [49] with modified metasurfaces as their primary radiators achieve the bandwidths of wider than 13.85% (24.2–27.8 GHz) and 11.3% (36.7–41.1 GHz), respectively. Therefore, it is a great challenge to realize mmW DBDP antenna array combining the merits of wide bandwidths, compact sizes, stable radiation performance, and beam scanning ability.

In this article, as illustrated in Fig. 1, a DBDP four-element microstrip antenna array with broadside radiation is proposed by utilizing two layers of gridded patches with triple groups of via-fences. Symmetric radiating and feeding structures support

Manuscript received December 24, 2020; revised February 24, 2021; accepted March 16, 2021. Date of publication April 6, 2021; date of current version October 6, 2021. This work was supported in part by the National Natural Science Foundation of China under Grant 62022045, in part by the Youth Top Program of Beijing Outstanding Talent Funding Project, in part by the National Key Research and Development Program of China under Grant 2018YFB1801603, and in part by Huawei Technologies. (Corresponding author: Yue Li.)

Wangyu Sun, Yue Li, Hao Li, and Xu Qin are with the Department of Electronic Engineering, Beijing National Research Center for Information Science and Technology, Tsinghua University, Beijing 100084, China (e-mail: lyee@tsinghua.edu.cn).

Le Chang was with the Consumer Business Group, Huawei Inc., Beijing 100095, China. He is now with the School of Information and Communications Engineering, Xi'an Jiaotong University, Xi'an 710049, China (e-mail: changle4015@126.com).

Hanyang Wang is with the Consumer Business Group, Huawei Inc., Reading RG2 6UF, U.K. (e-mail: hanwanga@gmail.com).

Color versions of one or more figures in this article are available at <https://doi.org/10.1109/TAP.2021.3070185>.

Digital Object Identifier 10.1109/TAP.2021.3070185

two orthogonal polarizations. The upper gridded patch operates as the main radiator, fed through the cross-shaped coupling slot. The TM_{10} and antiphase TM_{20} modes are excited at 27 and 45 GHz, respectively. By appropriately arranging the lower parasitic gridded patch, the input impedances of these two modes are matched simultaneously for dual-band coverage with wide bandwidth and high port isolation. Three groups of via-fences are properly designed for multiple goals, including bandwidth enhancement, surface wave suppression, and sidelobe level reduction. A prototype of the proposed 2×2 array has been fabricated with dimensions of $16.5 \times 16.5 \times 2.078 \text{ mm}^3$. Measured results show the wide bandwidths of 30.5% for the lower band and 9% for the higher band with average gains of 12 and 13.1 dBi. Meanwhile, a scanning range of $-51^\circ \sim 43^\circ$ at 27 GHz and $-28^\circ \sim 30^\circ$ at 45 GHz is obtained. The proposed DBDP antenna array has advantages of broadband, compact size, and competitive radiation performances.

II. ANTENNA CONFIGURATION AND WORKING MECHANISM

A. General Configuration of Antenna Array

As illustrated in Fig. 1(a), the proposed antenna array is designed by the multilayer printed circuit board (PCB) process. It consists of four dielectric layers (Dielectrics 1–4), three prepreg layers (Prepreg 1–3), and six metal layers (upper gridded patches, lower gridded patches, ground, feeding for y -direction polarization (Pol- y), feeding for x -direction polarization (Pol- x), and reflector). Dielectrics are constructed by Taconic TLY-5 with $\epsilon_r = 2.2$ and $\tan\delta = 0.0009$ (measured at 10 GHz). Dielectrics 1–3 have identical heights of 0.508 mm, and Dielectric 4 has a height of 0.254 mm. Prepreg materials are with the same thicknesses of 0.1 mm and are constructed by Taconic FR-28 with $\epsilon_r = 2.8$ and $\tan\delta = 0.004$ (measured at 10 GHz). Fig. 1(b) plots the side view. In Fig. 2, the detailed configurations are shown. Both the upper and lower gridded patch arrays are formed by four antenna elements that are arranged as 2×2 placement. For the upper patch array, each antenna element contains 4×4 subpatches, while for the lower patch array, it contains 2×2 subpatches. The double-layer gridded patches in Fig. 2(a) are with symmetrical structures. The dual-polarized characteristic is achieved by exciting the orthogonal coupling slots etched on the ground layer, as illustrated in the partially enlarged view of Fig. 2(b). As shown in Figs. 1(a) and 2(c), beneath these slots, two groups of Y-shaped feeding lines are placed in different layers to avoid intersections. Feeding lines for Pol- x are printed on the top layer of Dielectric 4, while those for Pol- y are printed on the bottom layer of Dielectric 3. Their distance along z -axis is $h_p = 0.1 \text{ mm}$. The asymmetry on feeding lines may lead to slight inconsistency on bandwidths of two polarizations. Several groups of via-fences are designed for multiple objectives and the layout is depicted in Figs. 1(b) and 2(d) in detail. The brown via-fence (Fence 3) is metalized through vias, which run through the whole structure from the reflector layer to the top layer. The blue (Fence 1), red (Fence 2), and green via-fences are metalized blind vias drilled from the reflector layer to

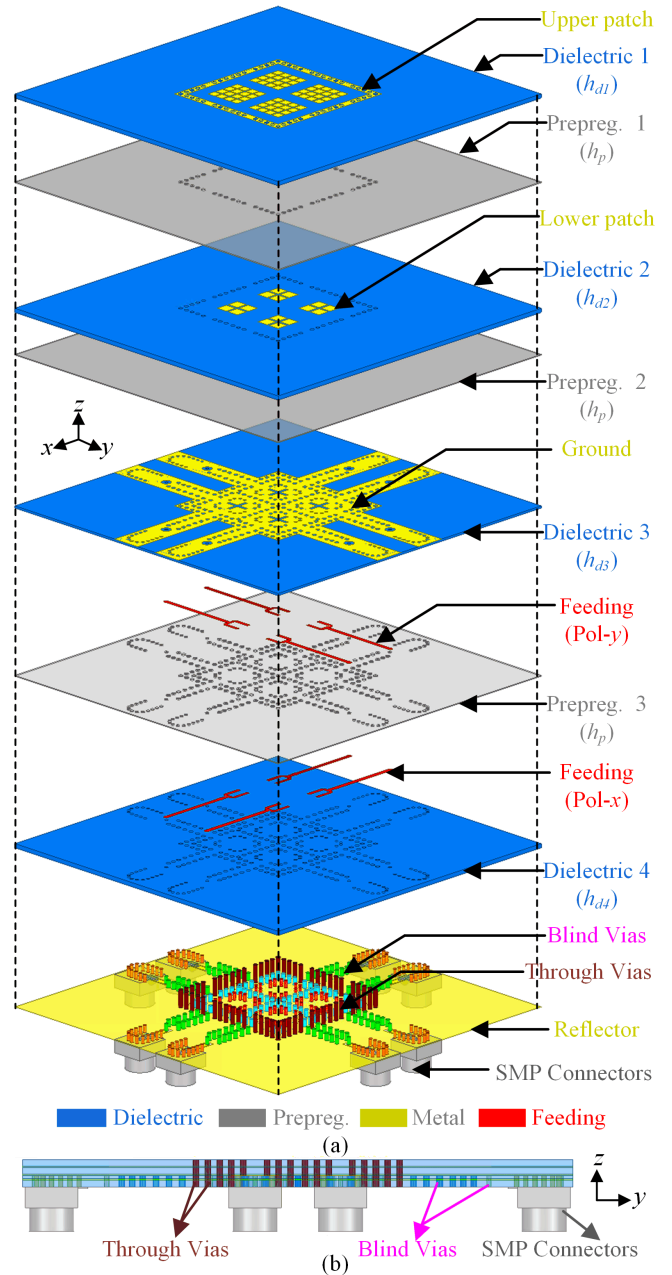


Fig. 1. Geometry of the proposed antenna array. (a) 3-D exploded view. (b) Side view.

the ground layer. The green blind-vias and red metal strips are assembled to design the substrate integrated coaxial line (SICL) [50]–[53], performing as the transmission line between 50Ω Mini-SMP connectors and Y-shaped metal strips. Eight green blind vias placed at the end of red metal strips provide the energy transferring paths from the connectors to the array. Some of this array's dimensions are listed in Table I, and the others are marked in Fig. 2.

B. Working Mechanism of Antenna Element

For expounding the working mechanism of the proposed array, a single antenna element is studied in this part. As illustrated in Fig. 3(a), the overall structure is the same as the array

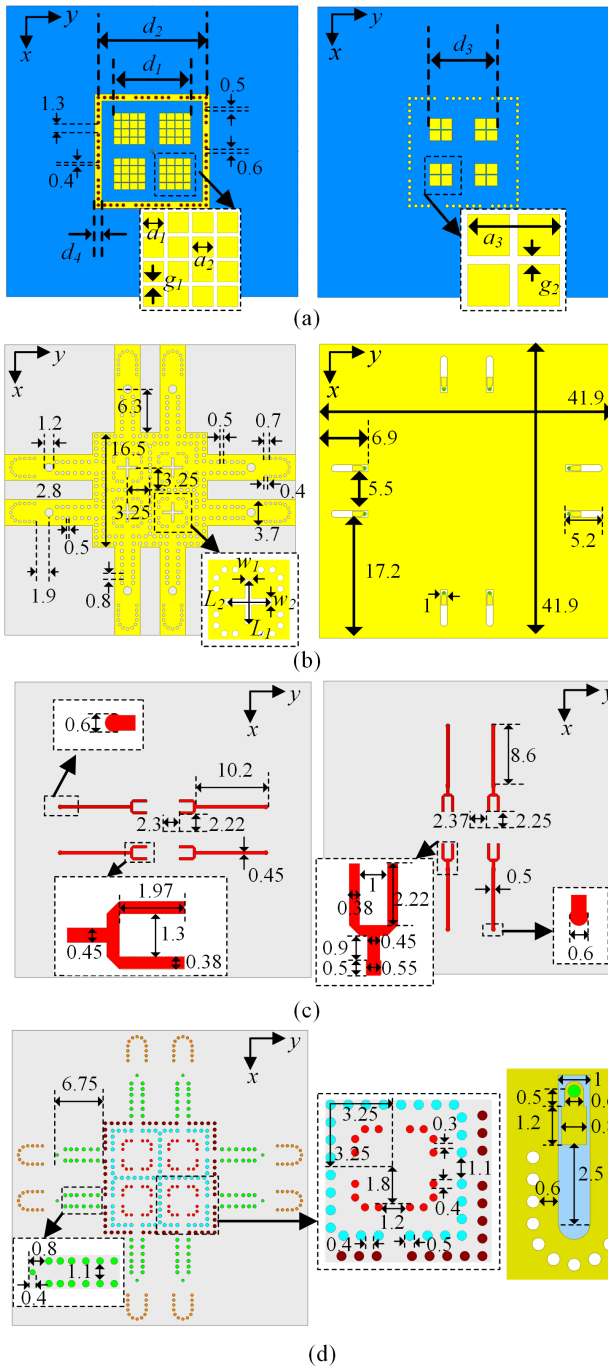


Fig. 2. Configuration of the proposed antenna array. (a) Upper and lower gridded patches. (b) Ground and reflector. (c) Feeding lines for Pol-y and Pol-x. (d) Via-fences and connector.

TABLE I

DIMENSIONS OF THE PROPOSED ARRAY (UNIT: MILLIMETERS)

h_{d1}	h_{d2}	h_{d3}	h_{d4}	h_p	d_1	d_2	L_1	L_2
0.508	0.508	0.254	0.508	0.1	11	15.5	2.8	2.9
d_3	d_4	a_1	a_2	a_3	g_1	g_2	w_1	w_2
9.7	1	1	1.1	3.2	0.1	0.15	0.4	0.4

in Fig. 1(a). Dielectrics are with a size of $10 \times 10 \text{ mm}^2$. For simplicity, only part of Y-shaped metal strips is reserved and their structures are presented in Fig. 3(b). Two metal strips

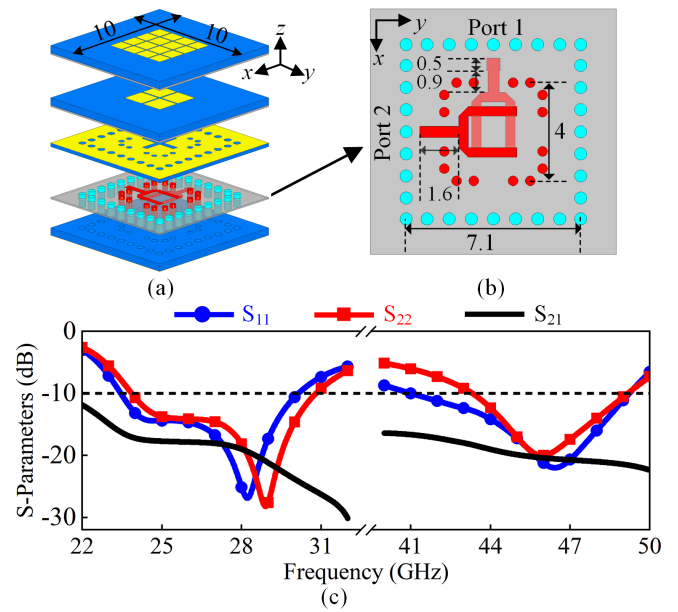


Fig. 3. Structure and simulated results of the antenna element. (a) 3-D exploded view, (b) feeding structure, and (c) simulated S-parameters, which indicates that two different resonant modes are excited around 27 and 45 GHz to achieve dual-band performance.

are fed with ideal 50Ω lumped port 1 and port 2. Fig. 3(c) reports the simulated S-parameters. Dual wide bandwidths are observed for two orthogonal polarizations. Simulated -10 dB impedance bandwidths are 23.8–30.2 and 43.3–49.2 GHz. High isolations are realized with S_{21} lower than -17.1 dB over the lower band and -18.3 dB over the higher band.

The operating principle and performance of Pol-x and Pol-y are almost the same. Therefore, only Pol-x is taken as an example in the following analyses. For demonstrating the resonant modes in two operating bands, sectional vector E -field distributions on the plane of $y = -0.1 \text{ mm}$ are shown in Fig. 4. It is found that for 25 and 27 GHz, their E -field distributions between the upper 4×4 gridded patch and ground are similar, and both exhibit the half-wavelength resonance along x -axis, which is consistent with conventional TM_{10} mode. Accordingly, E -field distributions at 45 and 47 GHz are both with the one-wavelength resonance along x -axis. Conventional TM_{20} mode is with in-phase E_z components in the central area and produces the undesired split radiation pattern. However, benefitting from the slot-excitation and gridded patches, the TM_{20} mode at 45 and 47 GHz in Fig. 4 is with out-of-phase E_z components in the central area and realizes the desired broadside radiation. Thus, the resonant mode in the higher band is named antiphase TM_{20} mode. Although researches about antiphase TM_{20} mode have been reported in [46]–[48], limited by their single-layer patch, these works can only make TM_{10} and antiphase TM_{20} modes operate in a single band with bandwidths less than 41%. It is hard to cover 24.25 and 47 GHz at the same time (relative bandwidth is about 63.8% from 24.25 to 47 GHz). To solve this difficulty, for the first time, the proposed work applies the double-layer gridded radiating patches and succeeds in making TM_{10} and antiphase TM_{20} modes cover two separated wide bands, respectively. In addition, frequencies of two

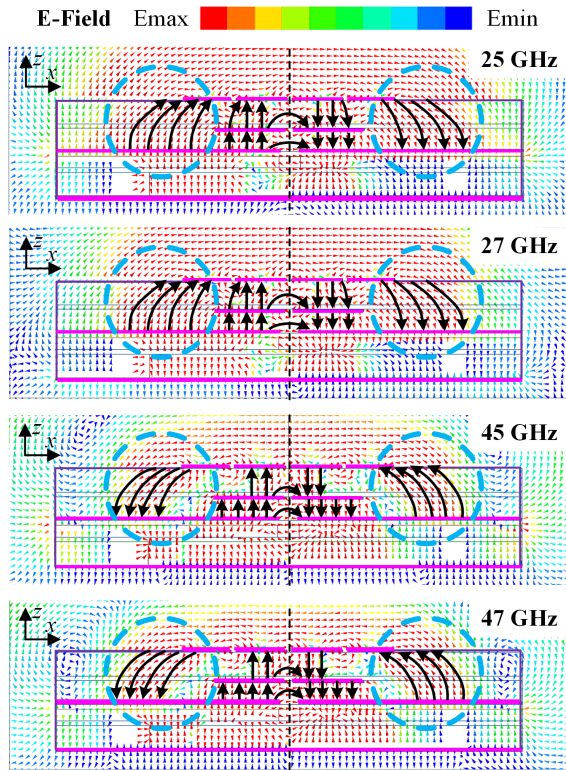


Fig. 4. Vector E -field distributions of the element in plane $y = -0.1$ mm at 25, 27, 45, and 47 GHz. (Pol- x as example). TM_{10} mode is excited at 25 and 27 GHz; antiphase TM_{20} mode is excited at 45 and 47 GHz.

operating bands can be easily adjusted to meet different system requirements, indicating the proposed antenna has the potential to be applied in a wider scope of work. Therefore, structures, operating mechanism, and application scenarios of the proposed antenna have obvious novelties and huge differences over previous works. Detailed discussions are presented in Sections II-C and II-D.

C. Analysis of the Double-Layer Gridded Patches

To investigate the functions of the double-layer gridded patches, Ant. 1 without the lower parasitic patch and Ant. 1-1 using a whole square patch as the lower parasitic patch are presented in Fig. 5(a) to compare with the proposed element. Simulated reflection coefficients and impedance properties are shown in Fig. 5(b) and (c), respectively. For Ant. 1, two resonant modes also appear at around 27 and 45 GHz, indicating that the upper patch is crucial in realizing dual-band performance. However, its impedance curves in Smith Chart are unmatched and bandwidths are very narrow. It is mainly because the distance between the single upper patch and the coupling slot is too far to effectively excite the two operating modes. The simulated sectional vector E -field distributions of Ant. 1 in xz plane at 27 and 45 GHz are depicted in Fig. 6(a). Comparing with that in Fig. 4, the E -fields in the central region of Ant. 1 are strongly destroyed by the coupling slot's radiation fields. The lower parasitic patch in the proposed antenna performs as a "bridge" between the slot and the upper gridded patch. The energy radiating from

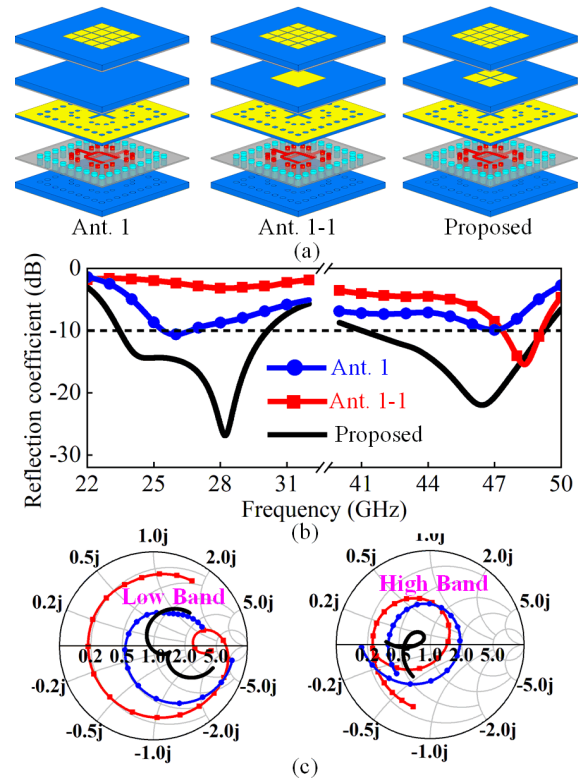


Fig. 5. Comparisons of Ant. 1 (only with the upper patch), Ant. 1-1 (using a whole square patch as the lower patch), and the proposed element. (a) Antenna structures, (b) simulated reflection coefficients, and (c) impedance properties. (Pol- x as example). It indicates that introducing 2×2 subpatches as the second layer greatly improves the bandwidths in the two bands simultaneously.

the slot is coupled to the lower patch at first, and then the upper patch is excited through the lower one. Therefore, more uniform and stable E -field distributions at lower and higher bands are achieved and help to support wider bandwidths. The lower patch also provides additional reactance and the input impedance can be optimized by tuning its dimensions. As a result, in Fig. 5(c), the impedance curves within a wide frequency range are moved to the center matching point and bandwidths are enhanced obviously in two bands simultaneously. In addition, it should be noted that choosing 2×2 gridded subpatches as the second layer is a novel and well thoughtful decision. Compared with a whole square patch in Ant. 1-1, the proposed subpatches provide more tuning freedom degrees (such as the size of subpatches and the size of gaps), making it easier to optimize bandwidths of two separated bands simultaneously. Besides, gaps between each subpatch provide additional capacitance to tuning the antenna's input impedances. In Fig. 5(b) and (c), it can be observed that it is difficult to realize wide bandwidths in two required bands simultaneously by just tuning the size W_3 of the whole square patch.

As the phases of E -fields radiated by the upper patch and the slot are opposite at 45 GHz, field cancellation phenomenon at broadside is observed in Ant. 1 and the broadside radiation deteriorates dramatically. For the proposed antenna, the slot's radiation is suppressed by the lower patch. Therefore, the broadside directivity increases by about 5 dB at 45 GHz,

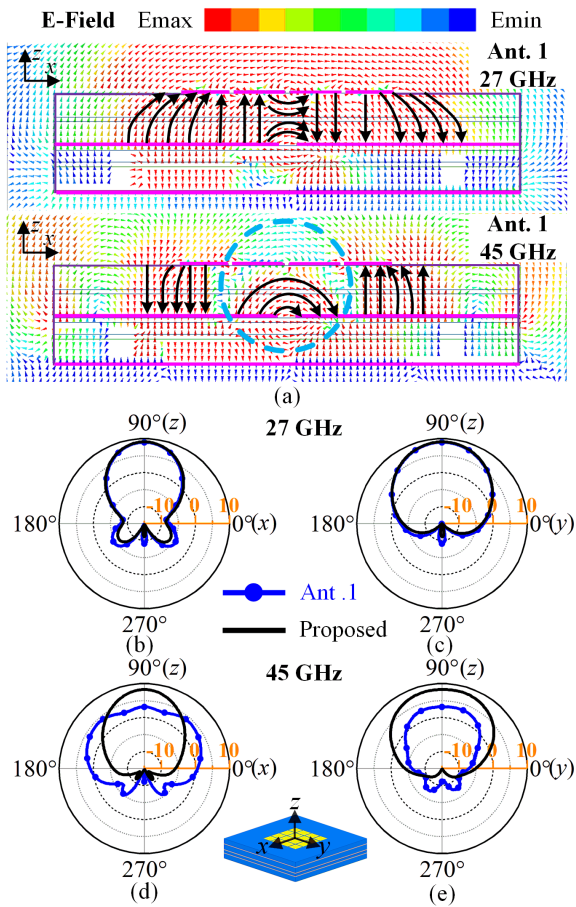


Fig. 6. (a) Vector E -field distributions of Ant. 1 in plane $y = -0.1$ mm at 27 and 45 GHz (Pol- x as example). Simulated directivities of Ant. 1 and the proposed antenna element in (b) xz plane and (c) yz plane at 27 GHz, and in (d) xz plane and (e) yz plane at 45 GHz. The 2×2 gridded patch in the proposed antenna suppresses the radiation of coupling slot and improves the antenna radiation directivity at 45 GHz.

as shown in Fig. 6(d) and (e). Meanwhile, the patterns at 27 GHz of Ant. 1 are almost the same as the ones of the proposed element, as depicted in Fig. 6(b) and (c). The reason is that the E -fields of the upper patch and coupling slot are in-phase.

The double-layer gridded patches have the ability to flexibly adjust operating frequencies of two bands. As depicted in Fig. 7(a), when the size a of the upper gridded patch becomes larger (smaller), resonant frequencies of TM_{10} and antiphase TM_{20} modes shift toward lower (higher) frequency simultaneously, so do two operating bands. In Fig. 7(b), the size a_3 of lower gridded patch has slight effect on the frequencies of the lower band, but has obvious effect on the higher band. When a_3 becomes larger (smaller), resonant frequency of antiphase TM_{20} mode shifts toward higher (lower) frequency. Therefore, by properly optimizing sizes of double-layer gridded patches, frequencies of two bands can be flexibly designed to meet different requirements. Finally, optimized values of $a = 4.5$ mm and $a_3 = 3.2$ mm are selected in this work.

D. Analysis of the Blind-Via Fences (Fence 1 and Fence 2)

As illustrated in Fig. 3, the proposed antenna element contains two groups of blind-via fences (Fence 1 and Fence 2).

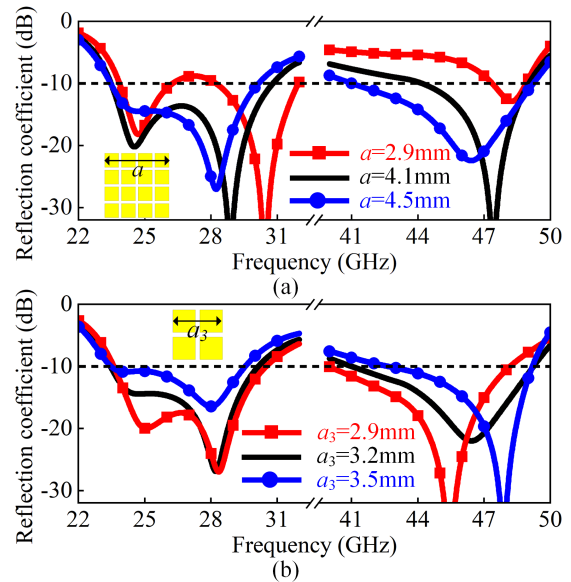


Fig. 7. Simulated reflection coefficients of the proposed element (Pol- x as example) with different values of (a) a for the upper patch and (b) a_3 for the lower parasitic patch. Upper patch affects frequencies of two bands simultaneously and lower patch mainly affects the frequency of higher band.

In Fig. 8, Ant. 2 without any fence and Ant. 3 only with Fence 1 are investigated to compare with the proposed antenna. In Fig. 8(b)–(d), simulated reflection coefficients, radiation efficiencies, and radiating directivities of the three antennas are presented. It is observed that Ant. 2 is with the worst reflection coefficient and high levels of backlobes and sidelobes. For Ant.3, the added Fence 1 makes the whole feeding structures surrounded in a closed cavity, avoiding energy leakage and radiation. Clear broadside radiation patterns with low sidelobes and backlobes are realized, as plotted in Fig. 8(d). Although Fence 1 improves the impedance matching to some extent, the bandwidths of Ant.3 are still very narrow. Then, Fence 2 is added around the coupling slot, performing as parasitic loads to optimize the impedance properties. By carefully adjusting the sizes and positions of Fence 1 and Fence 2, the coupling slot and gridded patches are effectively excited. In Fig. 8(c), compared with Ant. 2 and Ant. 3, the radiation efficiencies of the proposed antenna are also improved in two bands simultaneously with aids of Fence 2 and Fence 3. As a result, two wide bandwidths with consistent in-band radiation performances are achieved.

III. FOUR-ELEMENT ANTENNA ARRAY DESIGN

Based on the antenna element, a 2×2 DBDP antenna array is designed to realize high gain and beam scanning ability. The distances between adjacent elements are 6.5 mm (around $0.585\lambda_0$ at 27 GHz and $0.974\lambda_0$ at 45 GHz, λ_0 is the wavelength in free space). To achieve compact size and broadside radiation performance, the positions of the Fence 1 and Fence 2 are slightly adjusted, and another group of via fence in brown (Fence 3) is newly introduced. Besides, in consideration of the measurement conditions, SICLs are constructed. Configurations and dimensions of the final design are depicted in Fig. 2 and Table I.

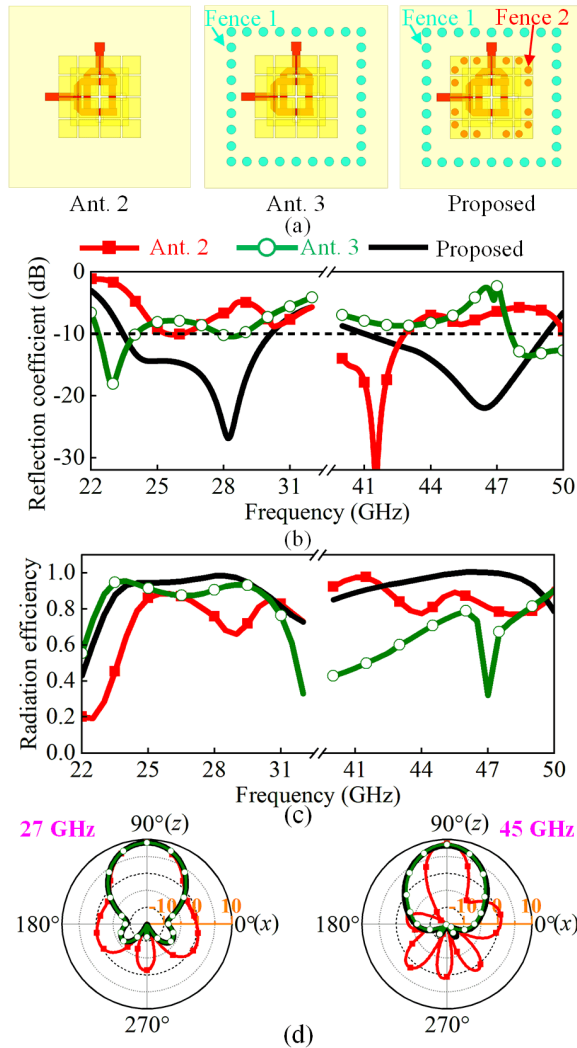


Fig. 8. Comparison of Ant. 2 without any blind-via fence, Ant. 3 only with the blue blind-via fence (Fence 1), and the proposed element with two groups of blind-via fences (Pol- x as example). (a) Top perspective views, (b) simulated reflection coefficients, (c) simulated radiation efficiencies, and (d) simulated directivities in xz plane. It indicates that Fence 1 mainly improves radiation patterns and Fence 2 mainly improves reflection coefficients.

A. Analysis of the Through-Via Fence (Fence 3)

Array 1 and Array 2 presented in Fig. 9(a) and (b) are used to investigate the performance differences in situations without or with Fence 3. Ports (P1, P4, P5, and P8) are used for the excitation of Pol- x , and ports (P2, P3, P6, and P7) for Pol- y . As shown in Fig. 9(c), simulated reflection coefficients of two arrays in the lower and higher band are similar, indicating that Fence 3 has little effect on impedance bandwidths.

Fig. 10 illustrates their simulated radiation patterns in xz plane and yz plane at 27 and 45 GHz. For Pol- x , to achieve broadside radiation, ports (P1, P4, P5, and P8) are excited with the phase distributions of $(0^\circ, 180^\circ, 180^\circ, \text{and } 0^\circ)$. The radiation patterns of Array 1 and Array 2 at 27 GHz are almost identical, while those at 45 GHz have obvious differences. It is because the electrical distance from the ground to the upper patch at 45 GHz is around two times than that at 27 GHz; thus, the surface wave at 45 GHz is harder to constrain.

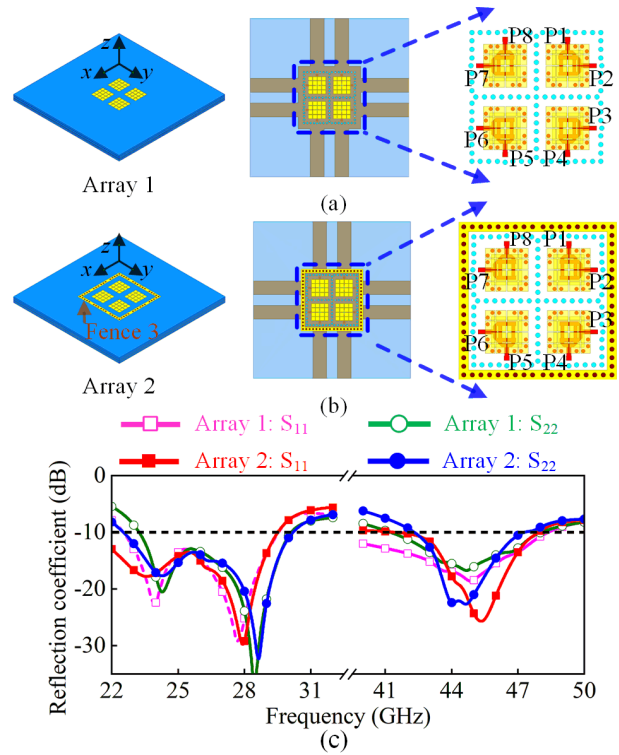


Fig. 9. Comparison of Array 1 without the brown Fence 3 and Array 2 with the brown Fence 3. Structures of (a) Array 1 and (b) Array 2. (c) Simulated reflection coefficients of these two arrays. Their bandwidths agree very well, indicating that Fence 3 has little effect on the input impedances.

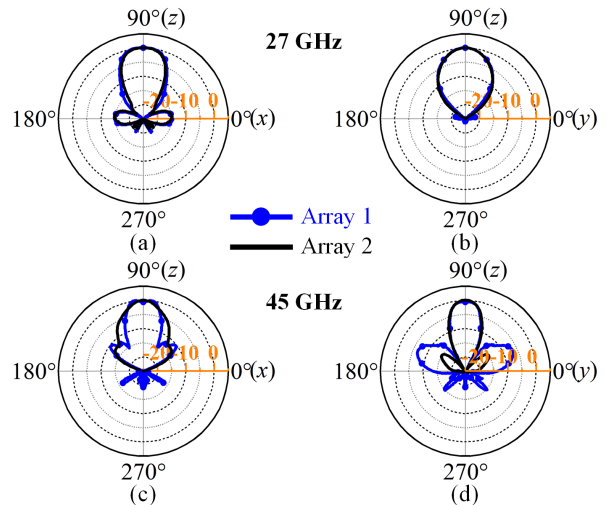


Fig. 10. Simulated normalized radiation patterns of Array 1 and Array 2 in xz plane and yz plane. (a) xz plane and (b) yz plane patterns at 27 GHz. (c) xz plane and (d) yz plane patterns at 45 GHz. [Pol- x as example, and with the phase distribution of (P1, P4, P5, and P8) = $(0^\circ, 180^\circ, 180^\circ, \text{and } 0^\circ)$]. Sidelobes at 45 GHz are reduced, because Fence 3 suppresses the radiation of surface wave.

It leads to stronger energy leakage at edges of ground plane at 45 GHz, resulting in higher sidelobes than 27 GHz, as shown in Fig. 10(b) and (d). The function of Fence 3 is to suppress radiation of surface wave. As the energy leakage at 27 GHz in Array 1 is very weak, its sidelobes in Array 2 do not get obvious improvement, even though Fence 3 is added. On the contrary, as the energy leakage at 45 GHz in array is much

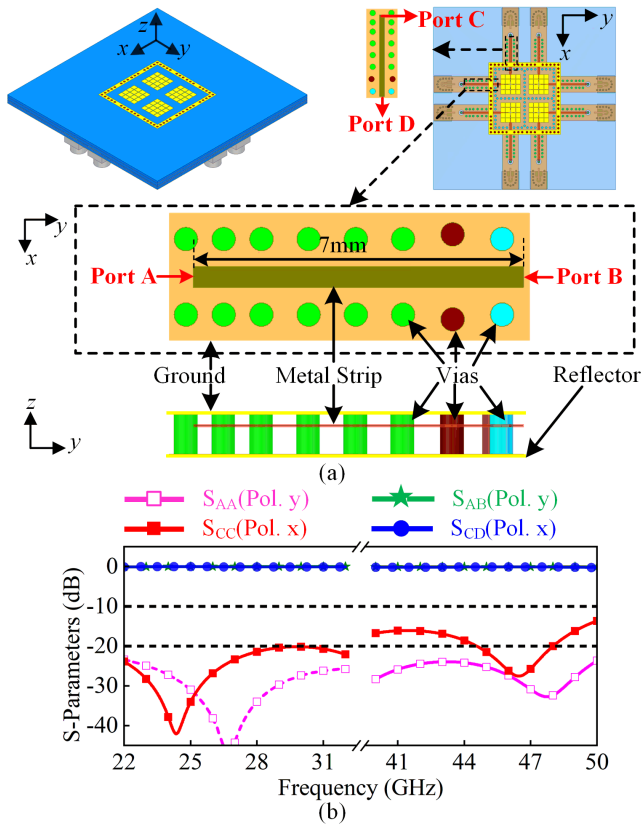


Fig. 11. Structures and performance of the SICLs for the final fabricated prototype. (a) Structures and (b) simulated S-parameters. It indicates that the SICLs are with merits of low transmission loss and broadband performance.

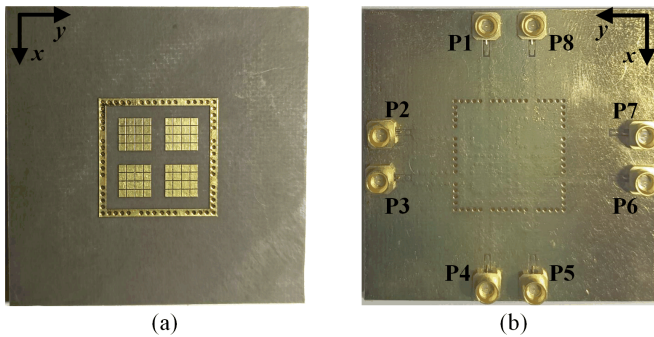


Fig. 12. Fabricated antenna array prototype. (a) Top view and (b) bottom view.

strong, its sidelobes in Array 2 are greatly suppressed by Fence 3 and the level is reduced from -6.8 to -15.1 dB in Fig. 10(d). As a result, Fence 3 provides an effective method to obtain low sidelobe characteristic, which is crucial in realizing beam scanning ability in 5G mmW arrays.

B. Substrate Integrated Coaxial Line

Taking Pol-y as an example, detailed structures of SICLs are illustrated in Fig. 11(a). The metal strip sandwiched between the reflectors and the ground is shown in Fig. 11. Two columns of metallic blind vias are drilled on both sides of the strip. Port A and Port B are connected with the SMP connector and Y-shaped metal strip, respectively. Although the SICL for

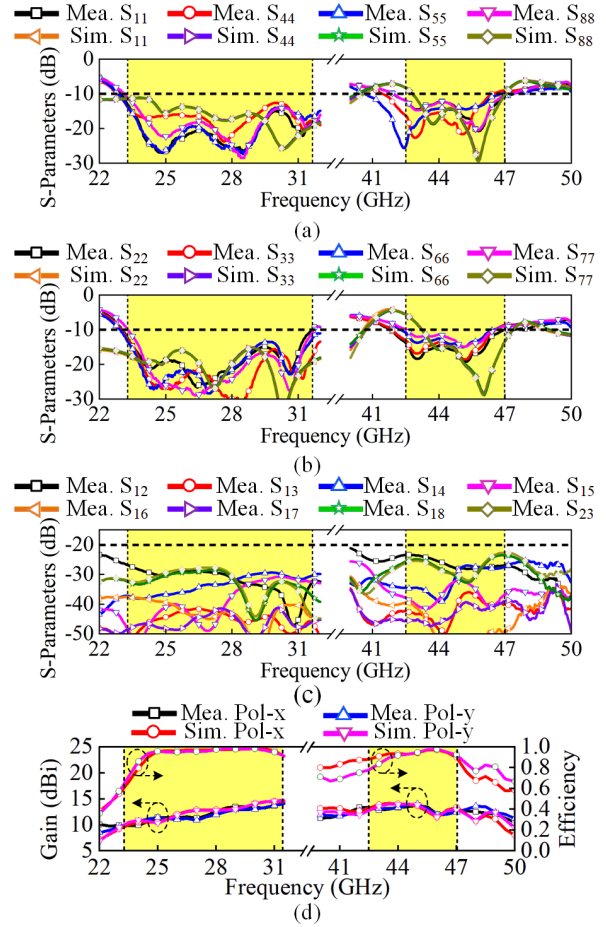


Fig. 13. Simulated and measured results of the proposed array. (a) Reflection coefficients of Pol-x (P1, P4, P5, and P8), (b) reflection coefficients of Pol-y (P2, P3, P6, and P7), (c) mutual couplings, and (d) gains and efficiencies, when the beam is steered at the z-direction.

Pol-x is not shown clearly in Fig. 11(a), its performances are also investigated, and its two ports are marked as port C and port D. When impedances of ports A–D are all set as 50Ω , simulated S-parameters are presented in Fig. 11(b). The slight discrepancy between Pol-x and Pol-y is caused by that their metal strips are with different heights. It is observed that S_{AA} and S_{CC} are better than -20 dB over 22–32 GHz and better than -14 dB over 40–50 GHz. S_{AB} and S_{CD} are almost equal to 0 dB in two bands, verifying that the SICLs employed for the measurements are with the merits of low transmission loss and broadband performance.

IV. FABRICATION AND MEASUREMENTS

A 2×2 array prototype is fabricated with multi-layer PCB process and is measured to verify its performances. The photograph of the prototype is illustrated in Fig. 12. Ports (P1, P4, P5, and P8) for Pol-x are with initial phase distribution of $(0^\circ, 180^\circ, 180^\circ, \text{ and } 0^\circ)$ and ports (P2, P3, P6, and P7) for Pol-y with initial phase distribution of $(0^\circ, 0^\circ, 180^\circ, \text{ and } 180^\circ)$. The S-parameters are measured with a vector analyzer (Agilent N5247A) and the radiation properties are tested in an anechoic chamber. Fig. 13(a) and (b) shows the reflection coefficients. The measured overlapped frequency bandwidths

TABLE II
PERFORMANCE COMPARISON OF MILLIMETER-WAVE ANTENNAS

Ref.	Element number	Bandwidth	Size ($\lambda_t \times \lambda_t$)	Height (λ_t^*)	Peak gain (dBi)	Polarization	Average efficiency	3dB scanning range
[14]	1×16	24.4-31.1 GHz (24.4%)	1.42×8.07	0.10	19.88	Single-Linear	~86%	-49°~59°@26 GHz
[30]	1×1	23.7-29.2 GHz (20.7%) 36.7-41.1 GHz (11.3%)	0.82×0.82	0.18	7.2/10.9	Single-Linear	~80% (simulation)	N.M.**
[31]	1×4	26.7-30.4 GHz (12.8%) 36.6-38.8 GHz (5.8%)	0.58×2.54	0.06	10.1/10.2	Single-Linear	~75.8%	N.M.
[32]	2×2	20.8-21.6 GHz (3.8%) 25.6-26.3 GHz (2.7%)	2.15×2.15	0.07	16/17.4	Single-Linear	>92% (simulation)	N.M.
[45]	2×2	27.1-29.5 GHz (8.4%) 36.1-38.3 GHz (5.9%)	3.07×3.25	0.34	13.1/13.2	Dual-Linear	~86.5% (simulation)	-18°~18°@28 GHz -18°~18°@38 GHz
[49]	2×2	24.2-27.8 GHz (13.9%) 36.9-42.8 GHz (14.8%)	1.61×1.61	0.20	14.5/16.5	Dual-Linear	~80%	N.M.
Proposed	2×2	23.3-31.7 GHz (30.5%) 42.5-46.5 GHz (9.0%)	1.28×1.28	0.16	14.8/14.1	Dual-Linear	~91.2% (simulation)	-51°~43°@27 GHz -28°~30°@45 GHz

* λ_t is the free-space wavelength at the starting frequency. **N.M.: Not Mentioned.

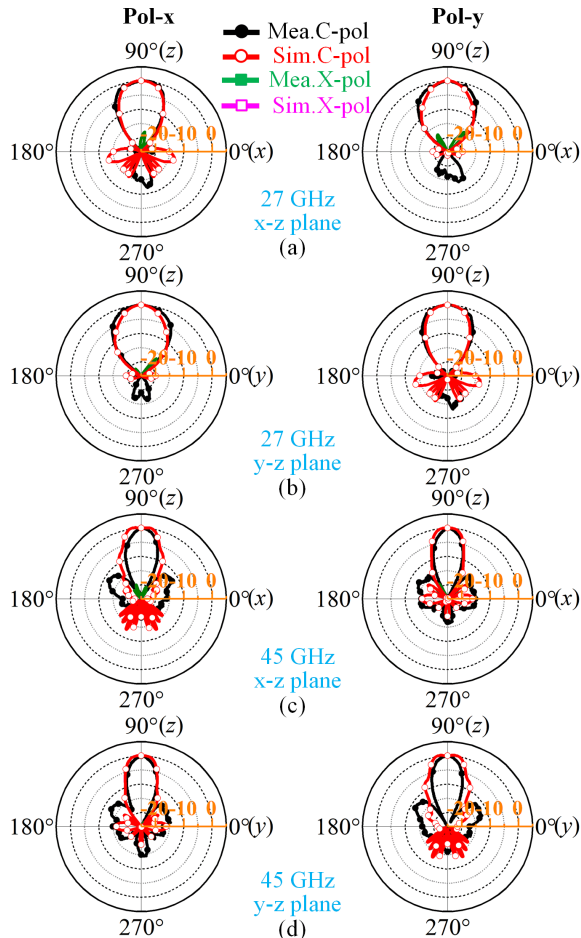


Fig. 14. Simulated and measured normalized radiation patterns of the antenna array for Pol-x and Pol-y at (a) 27 GHz in xz plane, (b) 27 GHz in yz plane, (c) 45 GHz in xz plane, and (d) 45 GHz in yz plane.

(reflection coefficients lower than -10 dB) for eight ports are 30.5% (23.3–31.7 GHz) in the lower band and 9% (42.5–46.5 GHz) in the higher band, which agree well with the simulated ones. Measured mutual couplings between P1 and

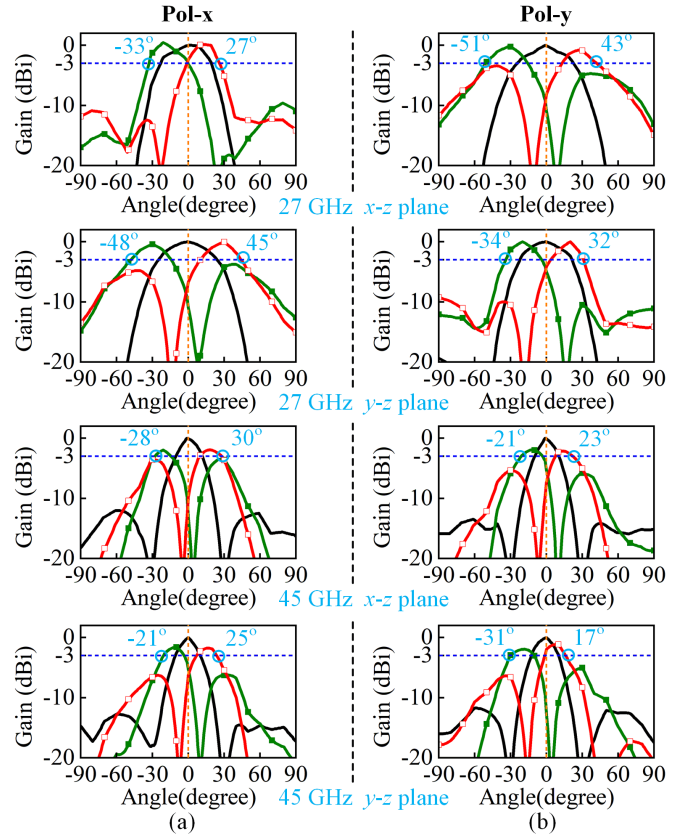


Fig. 15. Experimental 3 dB beam scanning performance of the proposed array in xz plane and yz plane at 27 and 45 GHz for (a) Pol-x and (b) Pol-y. The maximum 3 dB beam scanning ranges are $-51^\circ \sim 43^\circ$ at 27 GHz and $-28^\circ \sim 30^\circ$ at 45 GHz.

the other ports (P2–P8), and the one between P2 and P3 are reported in Fig. 13(c). Due to the structure symmetry, other mutual couplings are not presented here. The mutual couplings are lower than -26.9 dB across the lower band and -23.5 dB across the higher band.

Due to limitations of the measurement setup, the radiation performances of the four-element array (realized gain,

radiation patterns, and scanning ability) are obtained by computationally combining the individually measured, port-specific radiation performances of each antenna element in MATLAB. The beam-scanning array patterns have been calculated based on the measured radiation patterns of each element with different port phases [12], [54], [55]. When the beam points at $+z$ -axis, ports (P1, P4, P5, and P8) or (P2, P3, P6, and P7) are excited simultaneously and satisfy with the initial phase distributions mentioned above. In Fig. 13(d), the experimental gains of this array are shown and consistent with the simulated gains. The simulated average gains are 12.5 dBi for Pol- x , 12.6 dBi for Pol- y over the lower band, and 13.3 dBi for Pol- x and 13.2 dBi for Pol- y over the higher band. The experimental average gains are 12.2 dBi for Pol- x , 12 dBi for Pol- y over the lower band, and 13.1 dBi for Pol- x and 13.1 dBi for Pol- y over the higher band. Besides, simulated average efficiencies are 93.7% in the lower band and 91.2% in the higher band. The simulated and experimental normalized co- and cross-polarized radiation patterns at 27 and 45 GHz in xz plane and yz plane are shown in Fig. 14. Owing to the nearly symmetric configuration, the radiation patterns in xz plane/ yz plane of Pol- x are almost the same as the ones in yz plane/ xz plane of Pol- y . The measured results indicate that the array achieves the broadside radiation with low sidelobes of less than -20 dB at 27 GHz and -12 dB at 45 GHz. In this work, the antenna operates at the antiphase TM_{20} mode, which is equivalent to the combination two TM_{10} mode, with little effect on the efficiency and radiation pattern for higher band. Fig. 15 shows the experimental beam scanning performance. As the four antenna elements are placed by 2×2 , four main types of beam scanning (scan in xz plane for Pol- x , in xz plane for Pol- y , in yz plane for Pol- x , and in yz plane for Pol- y) are easily realized by applying various progressive phases. The maximum 3 dB beam scanning ranges are $-51^\circ \sim 43^\circ$ at 27 GHz and $-28^\circ \sim 30^\circ$ at 45 GHz. Slight asymmetric may be caused by the imperfect device installation and setup. The difference of scanning ability in the two bands is mainly caused by their different element spacings.

In Table II, the key characteristics of the proposed array are listed and compared with several mmW antennas in reported literature. Although the height or peak gains of the antenna in [14], [31], and [32] are better, their bandwidths and sizes are much worse than the proposed work and they can only realize single polarization. Metasurface-based antenna in [30] and [49] achieves broader bandwidth in higher band, but their narrower bandwidths in the lower band are not able to cover the 5G bands N257 and N258 simultaneously (24.25–29.5 GHz). They are also with larger dimensions. Besides, compared with published works, the proposed one also exhibits competitive efficiencies and 3 dB beam scanning ranges, which are two of significant performances in the design of mmW antennas.

V. CONCLUSION

In this article, a DBDP microstrip array is proposed with a low profile of $0.16\lambda_L$ and a compact size of $1.28\lambda_L \times 1.28\lambda_L$. By exploiting the double-layer gridded patches, two resonant modes are well excited in two desired bands,

respectively. Triple via-fences are properly designed to improve input impedance, radiation performances, and scanning ability. In addition, SICLs with low loss and broadband are employed for measurement. Simulated and experimental results show that it obtains two wide bandwidths of 30.5% and 9.0% with peak gains of 14.8 and 14.1 dBi for lower and higher bands, respectively. This array also provides a 3 dB beam scanning angles of $-51^\circ \sim 43^\circ$ at 27 GHz and $-28^\circ \sim 30^\circ$ at 45 GHz. The proposed array is with competitive properties of dual wide bandwidth, dual polarization, low profile, compact dimensions, and competitive beam scanning ability, exhibiting as a potential candidate for 5G mmW systems.

REFERENCES

- [1] J. G. Andrews *et al.*, "What will 5G be?" *IEEE J. Sel. Areas Commun.*, vol. 32, no. 6, pp. 1065–1082, Jun. 2014.
- [2] T. S. Rappaport *et al.*, "Millimeter wave mobile communications for 5G cellular: It will work!" *IEEE Access*, vol. 1, pp. 335–349, 2013.
- [3] W. Hong, K.-H. Baek, and S. Ko, "Millimeter-wave 5G antennas for smartphones: Overview and experimental demonstration," *IEEE Trans. Antennas Propag.*, vol. 65, no. 12, pp. 6250–6261, Dec. 2017.
- [4] J. Zhang, X. Ge, Q. Li, M. Guizani, and Y. Zhang, "5G millimeter-wave antenna array: Design and challenges," *IEEE Wireless Commun.*, vol. 24, no. 2, pp. 106–112, Apr. 2017.
- [5] A. Kumar and M. Gupta, "A review on activities of fifth generation mobile communication system," *Alexandria Eng. J.*, vol. 57, no. 2, pp. 1125–1135, Jun. 2018.
- [6] G. Lv, W. Chen, X. Chen, F. M. Ghannouchi, and Z. Feng, "A compact Ka/Q dual-band GaAs MMIC Doherty power amplifier with simplified offset lines for 5G applications," *IEEE Trans. Microw. Theory Techn.*, vol. 67, no. 7, pp. 3110–3121, Jul. 2019.
- [7] M. Khattak, A. Sohail, U. Khan, Z. Ullah, and G. Witjaksono, "Elliptical slot circular patch antenna array with dual band behaviour for future 5G mobile communication networks," *Prog. Electromagn. Res. C*, vol. 89, pp. 133–147, 2019. [Online]. Available: <https://www.jpier.org/PIERC/pier.php?paper=18101401>
- [8] Chinese Ministry of Industry and Information Technology Allocates Spectrum for the Fifth Generation Mobile Communication. Accessed: Nov. 15, 2017. [Online]. Available: <http://www.miit.gov.cn/n1146295/n1652858/n1652930/n3757020/c5907905/content.html>
- [9] Use of Spectrum Bands Above 24 GHz for Mobile Radio Services, document GN Docket 14-177, Notice Proposed Rulemaking, FCC Record 89A1, Jul. 2016.
- [10] J. Kurvinen, H. Kahkonen, A. Lehtovuori, J. Ala-Laurinaho, and V. Viikari, "Co-designed mm-wave and LTE handset antennas," *IEEE Trans. Antennas Propag.*, vol. 67, no. 3, pp. 1545–1553, Mar. 2019.
- [11] M. M. S. Taheri, A. Abdipour, S. Zhang, and G. F. Pedersen, "Integrated millimeter-wave wideband end-fire 5G beam steerable array and low-frequency 4G LTE antenna in mobile terminals," *IEEE Trans. Veh. Technol.*, vol. 68, no. 4, pp. 4042–4046, Apr. 2019.
- [12] H. Li, Y. Li, L. Chang, W. Sun, X. Qin, and H. Wang, "A wideband dual-polarized endfire antenna array with overlapped apertures and small clearance for 5G millimeter-wave applications," *IEEE Trans. Antennas Propag.*, vol. 69, no. 2, pp. 815–824, Feb. 2021.
- [13] J. Hu, Y. Li, S. Wang, and Z. Zhang, "Millimeter-wave air-filled slot antenna with conical beam based on bulk silicon MEMS technology," *IEEE Trans. Antennas Propag.*, vol. 68, no. 5, pp. 4077–4081, May 2020.
- [14] M. Khalily, R. Tafazolli, P. Xiao, and A. A. Kishk, "Broadband mm-wave microstrip array antenna with improved radiation characteristics for different 5G applications," *IEEE Trans. Antennas Propag.*, vol. 66, no. 9, pp. 4641–4647, Sep. 2018.
- [15] A. J. Abumunshar, N. K. Nahar, D. Hyman, and K. Sertel, "18–40 GHz low-profile phased array with integrated MEMS phase shifters," in *Proc. 11th Eur. Conf. Antennas Propag. (EUCAP)*, Paris, France, Mar. 2017, pp. 2800–2801.
- [16] A. J. Abumunshar, N. K. Nahar, K. Sertel, and D. J. Hyman, "K-to-Ka band low-profile phased array with integrated MEMS phase shifters," in *Proc. IEEE Int. Symp. Antennas Propag. (APSURSI)*, Fajardo, Puerto Rico, Jun. 2016, pp. 1143–1144.

- [17] N. Ashraf, O. M. Haraz, M. M. M. Ali, M. A. Ashraf, and S. A. S. Alshebili, "Optimized broadband and dual-band printed slot antennas for future millimeter wave mobile communication," *AEU-Int. J. Electron. Commun.*, vol. 70, no. 3, pp. 257–264, Mar. 2016.
- [18] Y. Zhou *et al.*, "Tightly coupled array antennas for ultra-wideband wireless systems," *IEEE Access*, vol. 6, pp. 61851–61866, 2018.
- [19] U. Farooq and G. M. Rather, "Design and analysis of dual band microstrip antenna for millimeter wave communication applications," *Int. J. Comput. Digit. Syst.*, vol. 9, no. 4, pp. 607–614, Jul. 2020.
- [20] M. Kaboli, M. S. Abrishamian, S. A. Mirtaheri, and S. M. Aboutorab, "High-isolation XX-polar antenna," *IEEE Trans. Antennas Propag.*, vol. 60, no. 9, pp. 4046–4055, Sep. 2012.
- [21] D. K. Sharma, S. Kulshrestha, S. B. Chakrabarty, and R. Jyoti, "Shared aperture dual-band dual polarization microstrip patch antenna," *Microw. Opt. Technol. Lett.*, vol. 55, no. 4, pp. 917–922, Apr. 2013.
- [22] X. W. Dai, Z. Y. Wang, X. C. Gao, G. Q. Luo, and Z. C. Hao, "Compact dual-broadband dual-polarized antenna with additional ground platform," *IEEE Access*, vol. 7, pp. 50650–50657, 2019.
- [23] Y. He, Z. Pan, X. Cheng, Y. He, J. Qiao, and M. M. Tentzeris, "A novel dual-band, dual-polarized, miniaturized and low-profile base station antenna," *IEEE Trans. Antennas Propag.*, vol. 63, no. 12, pp. 5399–5408, Dec. 2015.
- [24] Y. Liu, S. Wang, N. Li, J.-B. Wang, and J. Zhao, "A compact dual-band dual-polarized antenna with filtering structures for sub-6 GHz base station applications," *IEEE Antennas Wireless Propag. Lett.*, vol. 17, no. 10, pp. 1764–1768, Oct. 2018.
- [25] Y. Wang and Z. Du, "Dual-polarized dual-band microstrip antenna with similar-shaped radiation pattern," *IEEE Trans. Antennas Propag.*, vol. 63, no. 12, pp. 5923–5928, Dec. 2015.
- [26] X.-C. Lin and C.-C. Yu, "A dual-band CPW-fed inductive slot-monopole hybrid antenna," *IEEE Trans. Antennas Propag.*, vol. 56, no. 1, pp. 282–285, Jan. 2008.
- [27] I. Yeom, J. M. Kim, and C. W. Jung, "Dual-band slot-coupled patch antenna with broad bandwidth and high directivity for WLAN access point," *Electron. Lett.*, vol. 50, no. 10, pp. 726–728, May 2014.
- [28] S. H. S. Esfahlani, A. Tavakoli, and P. Dehkhoda, "A compact single-layer dual-band microstrip antenna for satellite applications," *IEEE Antennas Wireless Propag. Lett.*, vol. 10, pp. 931–934, 2011.
- [29] L. Wang, Y. J. Cheng, D. Ma, and C. X. Weng, "Wideband and dual-band high-gain substrate integrated antenna array for E-band multi-gigahertz capacity wireless communication systems," *IEEE Trans. Antennas Propag.*, vol. 62, no. 9, pp. 4602–4611, Sep. 2014.
- [30] T. Li and Z. N. Chen, "A dual-band metasurface antenna using characteristic mode analysis," *IEEE Trans. Antennas Propag.*, vol. 66, no. 10, pp. 5620–5624, Oct. 2018.
- [31] T. Deckmyn, M. Cauwe, D. V. Ginste, H. Rogier, and S. Agneessens, "Dual-band (28,38) GHz coupled quarter-mode substrate-integrated waveguide antenna array for next-generation wireless systems," *IEEE Trans. Antennas Propag.*, vol. 67, no. 4, pp. 2405–2412, Apr. 2019.
- [32] W. Li, K. D. Xu, X. Tang, Y. Yang, Y. Liu, and Q. H. Liu, "Substrate integrated waveguide cavity-backed slot array antenna using high-order radiation modes for dual-band applications in K-band," *IEEE Trans. Antennas Propag.*, vol. 65, no. 9, pp. 4556–4565, Sep. 2017.
- [33] L. E. Miller, "Why UWB? A review of ultrawideband technology," Wireless Commun. Technol. Group (WCTG), Gaithersburg, MD, USA, Tech. Rep., Apr. 2002. [Online]. Available: <http://citeseerx.ist.psu.edu/viewdoc/download?doi=10.1.1.76.7051&rep=rep1&type=pdf>
- [34] S.-T. Liu, Y.-W. Hsu, and Y.-C. Lin, "A dual polarized cavity-backed aperture antenna for 5G mmW MIMO applications," in *Proc. IEEE Int. Conf. Microw., Commun., Antennas Electron. Syst. (COMCAS)*, Tel Aviv-Yafo, Israel, Nov. 2015, pp. 1–5.
- [35] B. Feng, Y. Tu, J. Chen, S. Yin, and K. L. Chung, "Dual linearly-polarized antenna array with high gain and high isolation for 5G millimeter-wave applications," *IEEE Access*, vol. 8, pp. 82471–82480, 2020.
- [36] H. Chu and Y.-X. Guo, "A filtering dual-polarized antenna subarray targeting for base stations in millimeter-wave 5G wireless communications," *IEEE Trans. Compon., Package., Manuf. Technol.*, vol. 7, no. 6, pp. 964–973, Jun. 2017.
- [37] Z. Chen, H. Liu, J. Yu, and X. Chen, "High gain, broadband and dual-polarized substrate integrated waveguide cavity-backed slot antenna array for 60 GHz band," *IEEE Access*, vol. 6, pp. 31012–31022, 2018.
- [38] S.-G. Zhou, Z.-H. Peng, G.-L. Huang, J.-Y. Li, and C.-Y.-D. Sim, "Design of wideband and dual polarized cavity antenna planar array," *IEEE Trans. Antennas Propag.*, vol. 64, no. 10, pp. 4565–4569, Oct. 2016.
- [39] A. Alieldin, Y. Huang, S. J. Boyes, M. Stanley, S. D. Joseph, and B. Al-Juboori, "A dual-broadband dual-polarized fyfot-shaped antenna for mobile base stations using MIMO over-lapped antenna subarrays," *IEEE Access*, vol. 6, pp. 50260–50271, 2018.
- [40] Q. Hua, Y. Huang, A. Alieldin, C. Song, T. Jia, and X. Zhu, "A dual-band dual-polarized base station antenna using a novel feeding structure for 5G communications," *IEEE Access*, vol. 8, pp. 63710–63717, 2020.
- [41] B. Feng, L. Li, J.-C. Cheng, and C.-Y.-D. Sim, "A dual-band dual-polarized stacked microstrip antenna with high-isolation and band-notch characteristics for 5G microcell communications," *IEEE Trans. Antennas Propag.*, vol. 67, no. 7, pp. 4506–4516, Jul. 2019.
- [42] S. Lee, S. Kim, and J. Choi, "Dual-band dual-polarized proximity fed patch antenna for 28 GHz/39 GHz 5G millimeter-wave communications," in *Proc. 13th Eur. Conf. Antennas Propag. (EuCAP)*, Krakow, Poland, 2019, pp. 1–5.
- [43] Z. Siddiqui, M. Sonkki, J. Chen, M. Berg, M. E. Leinonen, and A. Parssinen, "Dual-band dual-polarized antenna for mm-wave 5G base station antenna array," in *Proc. 14th Eur. Conf. Antennas Propag. (EuCAP)*, Copenhagen, Denmark, Mar. 2020, pp. 1–4.
- [44] Y. He, M. Rao, Y. Liu, G. Jing, M. Xi, and L. Zhao, "28/39-GHz dual-band dual-polarized millimeter wave stacked patch antenna array for 5G applications," in *Proc. Int. Workshop Antenna Technol. (iWAT)*, Bucharest, Romania, Feb. 2020, pp. 1–4.
- [45] H.-N. Hu, F.-P. Lai, and Y.-S. Chen, "Dual-band dual-polarized scalable antenna subarray for compact millimeter-wave 5G base stations," *IEEE Access*, vol. 8, pp. 129180–129192, 2020.
- [46] W. Liu, Z. N. Chen, and X. Qing, "Metamaterial-based low-profile broadband aperture-coupled grid-slotted patch antenna," *IEEE Trans. Antennas Propag.*, vol. 63, no. 7, pp. 3325–3329, Jul. 2015.
- [47] W. Sun, Y. Li, Z. Zhang, and Z. Feng, "Broadband and low-profile microstrip antenna using strip-slot hybrid structure," *IEEE Antennas Wireless Propag. Lett.*, vol. 16, pp. 3118–3121, 2017.
- [48] W. Sun, Y. Li, Z. Zhang, and P.-Y. Chen, "Low-profile and wideband microstrip antenna using quasi-periodic aperture and slot-to-CPW transition," *IEEE Trans. Antennas Propag.*, vol. 67, no. 1, pp. 632–637, Jan. 2019.
- [49] B. Feng, X. He, J.-C. Cheng, and C.-Y.-D. Sim, "Dual-wideband dual-polarized metasurface antenna array for the 5G millimeter wave communications based on characteristic mode theory," *IEEE Access*, vol. 8, pp. 21589–21601, 2020.
- [50] F. Zhu, W. Hong, J.-X. Chen, and K. Wu, "Ultra-wideband single and dual baluns based on substrate integrated coaxial line technology," *IEEE Trans. Microw. Theory Techn.*, vol. 60, no. 10, pp. 3062–3070, Oct. 2012.
- [51] K. Xing, B. Liu, Z. Guo, X. Wei, R. Zhao, and Y. Ma, "Backlobe and sidelobe suppression of a Q-band patch antenna array by using substrate integrated coaxial line feeding technique," *IEEE Antennas Wireless Propag. Lett.*, vol. 16, pp. 3043–3046, 2017.
- [52] B. Liu *et al.*, "A novel slot array antenna with a substrate-integrated coaxial line technique," *IEEE Antennas Wireless Propag. Lett.*, vol. 16, pp. 1743–1746, 2017.
- [53] T. Zhang, Y. Zhang, W. Hong, and K. Wu, "Wideband millimeter-wave SIW cavity backed patch antenna fed by substrate integrated coaxial line," in *Proc. IEEE Int. Wireless Symp. (IWS)*, Mar. 2015, pp. 1–4.
- [54] R. M. Moreno, J. Ala-Laurinaho, A. Khripkov, J. Iivonen, and V. Viikari, "Dual-polarized mm-wave endfire antenna for mobile devices," *IEEE Trans. Antennas Propag.*, vol. 68, no. 8, pp. 5924–5934, Aug. 2020.
- [55] R. M. Moreno *et al.*, "Dual-polarized mm-wave endfire chain-slot antenna for mobile devices," *IEEE Trans. Antennas Propag.*, vol. 69, no. 1, pp. 25–34, Jan. 2021, doi: [10.1109/TAP.2020.3001434](https://doi.org/10.1109/TAP.2020.3001434).



Wangyu Sun (Graduate Student Member, IEEE) received the B.S. and M.S. degrees from Tsinghua University, Beijing, China, in 2016 and 2019, respectively, where he is currently pursuing the Ph.D. degree in electronic engineering.

His current research interests include broadband antennas, low profile antennas, millimeter-wave antenna arrays, metamaterials, and waveguide metatronics.

Mr. Sun is serving as a reviewer for the IEEE TRANSACTIONS ON ANTENNAS AND PROPAGATION, IEEE ANTENNAS AND WIRELESS PROPAGATION LETTERS, the IEEE SENSORS JOURNAL, and *Computer Applications in Engineering Education*.



Yue Li (Senior Member, IEEE) received the B.S. degree in telecommunication engineering from Zhejiang University, Hangzhou, China, in 2007, and the Ph.D. degree in electronic engineering from Tsinghua University, Beijing, China, in 2012.

He is currently an Associate Professor with the Department of Electronic Engineering, Tsinghua University. In 2012, he joined the Department of Electronic Engineering, Tsinghua University, as a Post-Doctoral Fellow. In 2013, he joined the Department of Electrical and Systems Engineering, University of Pennsylvania, Philadelphia, PA, USA, as a Research Scholar. He joined the Institute for Infocomm Research (I2R), A*STAR, Singapore, as a Visiting Scholar, in 2010, and also the Hawaii Center of Advanced Communication (HCAC), University of Hawai'i at Mānoa, Honolulu, HI, USA, in 2012. Since 2016, he has been with Tsinghua University, where he is currently an Assistant Professor. He has authored or coauthored over 150 journal articles and 45 international conference articles, and holds 23 granted Chinese patents. His current research interests include metamaterials, plasmonics, electromagnetics, nanocircuits, mobile and handset antennas, multiple input and multiple output (MIMO) and diversity antennas, and millimeter-wave antennas and arrays.

Dr. Li received the Issac Koga Gold Medal from the URSI General Assembly in 2017; the Second Prize of Science and Technology Award of the China Institute of Communications in 2017; the Young Scientist Awards from the conferences of PIERS 2019, ACES 2018, AT-RASC 2018, AP-RASC 2016, EMTS 2016, and URSI GASS 2014; the Best Paper Awards from the conferences of ISAP 2019, CSQRWC 2018, NCMMW 2018 and 2017, APCAP 2017, NCANT 2019 and 2017, ISAPE 2016, and ICMMT 2016; the Outstanding Doctoral Dissertation of Beijing Municipality in 2013; and the Principal Scholarship of Tsinghua University in 2011. He is serving as the Associate Editor for the IEEE TRANSACTIONS ON ANTENNAS AND PROPAGATION, IEEE ANTENNAS AND WIRELESS PROPAGATION LETTERS, *Microwave and Optical Technology Letters*, and *Computer Applications in Engineering Education*, and also as the Editorial Board Member of *Scientific Report*.



Le Chang (Member, IEEE) received the B.S. degree in electronics and information engineering from Xidian University, Xi'an, China, in 2012, and the Ph.D. degree in electrical engineering from Tsinghua University, Beijing, China, in 2017.

From 2017 to 2020, he was a Senior Engineer with the Antenna and RF Group, Huawei Device Ltd., Beijing. Since 2021, he has been a Special Appointed Researcher with Xi'an Jiaotong University, Xi'an. His current research interests include fifth-generation (5G) mobile antennas, millimeter-wave antennas, and beam scanning antennas.



Hao Li received the B.S. degree in electronic engineering from Tsinghua University, Beijing, China, in 2018, where he is currently pursuing the Ph.D. degree in electronic engineering.

His current research interests include wideband antennas, millimeter-wave antenna arrays, metamaterials, and metamaterial-inspired antennas.

Mr. Li serves as a reviewer for the IEEE TRANSACTIONS ON ANTENNAS AND PROPAGATION and the *Microwave and Optical Technology Letters*.



Xu Qin received the B.S. degree in electrical engineering from Tsinghua University, Beijing, China, in 2019, where he is currently pursuing the Ph.D. degree in electrical engineering.

His research interests include metamaterials, small antenna, and microstrip antenna.



Hanyang Wang (Fellow, IEEE) received the Ph.D. degree from Heriot Watt University, Edinburgh, U.K., in 1995.

From 1986 to 1991, he was a Lecturer and an Associate Professor with Shandong University, Jinan, China. From 1995 to 1999, he was a Post-Doctoral Research Fellow with the University of Birmingham, Birmingham, U.K., and also with the University of Essex, Colchester, U.K. From 1999 to 2000, he was a Software Development and Microwave and an Antenna Engineering Consultant Engineer with Vector Fields Ltd., Oxford, U.K. He joined Nokia U.K. Ltd., Farnborough, U.K., in 2001, where he had been a Mobile Antenna Specialist for 11 years. He joined Huawei Technologies, Reading, U.K., after leaving Nokia, and he is currently the Chief Mobile Antenna Expert and the Head of the Mobile Antenna Technology Division, Huawei Technologies. He leads a large group of antenna experts and engineers and takes the full leadership and responsibility in the research and development of antenna technologies to guarantee the market success of all Huawei's mobile terminal products ranging from smartphones, laptops, tablets, MiFi, data cards, smart watches, bluetooth (BT) headsets, routers, Internet of Things (IoT), smart screens, customer premise equipment (CPE), virtual reality (VR), and automobiles. He is also an Adjunct Professor with Nanjing University, Nanjing, China, and Sichuan University, Chengdu, China. He has authored over 110 referred articles on these topics. He holds over 50 granted U.S./EU/JP/CN patents, including 29 U.S. patents, and has other 60+ patent applications in pending. His current research interests include small, wideband, and multiband antennas for mobile terminals, multiple input and multiple output (MIMO) antennas, and antenna arrays for fifth-generation (5G) sub-6 GHz and 5G millimeter-wave mobile communications.

Dr. Wang is a fellow of Huawei and IET. He was a recipient of the Title of Nokia Inventor in 2005, the Nokia Excellence Award in 2011, the Huawei Individual Gold Medal Award in 2012, and the Huawei Team Gold Medal Award in 2013 and 2014, respectively. His patent was ranked number one among 2015 Huawei top ten patent awards. He has been an Associate Editor of IEEE ANTENNAS AND WIRELESS PROPAGATION LETTERS since 2015.